Title
Phase-resolved dynamic wavefront imaging of cilia metachronal waves.

Journal
Quantitative imaging in medicine and surgery, 13(4)

ISSN
2223-4292

Authors
Miao, Yusi
Jing, Joseph C
Chou, Lidek
et al.

Publication Date
2023-04-01

DOI
10.21037/qims-22-439

Peer reviewed

Original Article

Phase-resolved dynamic wavefront imaging of cilia metachronal waves

Yusi Miao[1,2]^, Joseph C. Jing[1], Lidek Chou[1], Zhikai Zhu[1,2], Brian J. F. Wong[1,2,3], Zhongping Chen[1,2]

[1]Beckman Laser Institute and Medical Clinic, University of California, Irvine, CA, USA; [2]Department of Biomedical Engineering, University of California, Irvine, CA, USA; [3]Department of Otolaryngology-Head and Neck Surgery, University of California, Irvine, CA, USA

Contributions: (I) Conception and design: Y Miao, JC Jing, BJF Wong, Z Chen; (II) Administrative support: Z Zhu, L Chou; (III) Provision of study materials or patients: Z Zhu, L Chou; (IV) Collection and assembly of data: Y Miao, L Chou, Z Zhu; (V) Data analysis and interpretation: Y Miao, JC Jing; (VI) Manuscript writing: All authors; (VII) Final approval of manuscript: All authors.

Correspondence to: Zhongping Chen. Beckman Laser Institute and Medical Clinic, 1002 Health Sciences Road East, Irvine, CA 92612-1475, USA. Email: z2chen@uci.edu.

Background: The coordination and the directional order of ciliary metachronal waves are the major factors that determine the effectiveness of mucociliary clearance (MCC). Even though metachronal waves play an essential part in immune response, clinical diagnostic tools and imaging techniques that can reliably and efficiently capture their spatial distribution and function are currently limited.

Methods: We present label-free high-speed visualization of ciliary metachronal wave propagations in freshly-excised tracheal explants using a spectrally-encoded interferometric microscope over a two-dimensional (2D) plane of 0.5 mm × 0.5 mm at an acquisition rate of 50 frame-per-second. Furthermore, phase-resolved enhanced dynamic (PHRED) analysis of time-series doppler images was performed, where spatial-temporal characteristics of cilia metachronal wave motions are revealed through frequency component analysis and spatial filtering.

Results: The PHRED analysis of phase-resolved Doppler (PRD) images offers a capability to distinguish the propagation direction of metachronal waves, and quantitatively assess amplitude and dominant frequency of cilia beating at each spatial location. Compared to the raw PRD images, the phase-resolved dynamic wavefront imaging (PRDWI) method showed the direction and coordination of collective cilia movement more distinctively.

Conclusions: The PRDWI technique can have broad application prospects for the diagnosis of human respiratory diseases and evaluation of the curative effect of treatments and open new perspectives in biomedical sciences.

Keywords: Cilia function; spatial-temporal analysis; metachronal waves; phase-resolved imaging; dynamic wavefront imaging

Submitted May 02, 2022. Accepted for publication Jan 19, 2023. Published online Mar 08, 2023.
doi: 10.21037/qims-22-439
View this article at: https://dx.doi.org/10.21037/qims-22-439

^ ORCID: 0000-0001-7368-240X.

Introduction

The upper airway's mucociliary clearance (MCC) system is essential in protecting against airborne pathogens by trapping viruses, bacteria, and other particles in mucus. The mucus, which forms the first barrier in the upper airway, is propelled out of the lungs by the cilia, small organelles on the surface of the airway, to remove trapped pathogens (1,2). Beneath the mucus are the cilia, surface organelles with a length of approximately 6–7 μm, and a diameter of 0.2–0.3 μm in the human airway, which provide the kinetic force to proximally propel the mucus in order to expel the trapped pathogens out of the lungs (3-5). To accomplish this important role, cilia displays a striking self-organized collective beating pattern in the form of metachronal waves mediated by multiple physiological regulators (6-8). To achieve metachronal synchronization and effective MCC, each cilium beats at the same characteristic beating frequency but in a phase-shifted manner compared to its neighbors. It is important to note that the propagation direction of the metachronal waves is not necessarily the same as the direction of cilia beating (6). When the MCC system is not functioning properly, it can lead to an increased risk for both acute and chronic respiratory illnesses such as cystic fibrosis, asthma, and chronic obstructive pulmonary disease. Despite the importance of MCC in the immune response, there are currently limited diagnostic tools and imaging techniques that can accurately measure the movement and function of the cilia.

The main challenge with visualizing metachronal waves, *in vivo*, is that imaging of dynamic cilia movements requires both cellular resolution and high imaging speed, limiting vast majority of current MCC characterization techniques to nasal brushing sampling (9,10), cell culturing (11-13), or movement tracking of radiolabeled markers (14,15). Although those studies capture certain features of MCC (e.g., beating frequency, MCC rate), most of those techniques are either invasive, slow to process, or require a bulky equipment. Most of all, the absence of standardization in sample handling and quantitative assessment of metachronal coordination limits its current clinical applicability. Over the years, new techniques to characterize MCC and cilia function in different spatial and temporal scales are proposed. For example, particle motion tracking using synchrotron X-ray imaging has been demonstrated as a mean to quantify mucociliary transport behavior in live animals (16-18). Furthermore, in recent years, there has been considerable interest in quantifying cilia beating and MCC function using high-resolution label-free optical imaging techniques such as optical coherence tomography (OCT) (19-27) and optical coherence phase microscopy (28-30). The depth-resolved imaging capability and low phototoxicity of OCT imaging makes it particularly suitable for quantifying ciliary activities along with other relevant physiological parameters. For example, using a high-resolution OCT endoscopic probe, Leung *et al*. extensively investigated cilia beating frequency (CBF) and morphological imaging of micro-anatomical features (e.g., periciliary liquid layer depth, airway surface liquid layer depth, epithelium thickness) of the upper airway in healthy and cystic fibrosis patients (21). Phase-resolved Doppler (PRD) OCT imaging, a functional extension of OCT, is another promising technique for quantifying ciliary activities. PRD OCT provides exceptional axial displacement by detecting Doppler frequency shift induced by the cilia movement (23,31,32). The main advantage of phase-resolve Doppler OCT imaging compared to conventional structural OCT imaging is that Doppler measurement is able to detect sub-micrometer displacement, which is smaller than the spatial resolution of the imaging system. However, most of the current OCT measurements of cilia dynamics are limited to a single cross-sectional scan location, as the imaging speed of current OCT is insufficient to visualize spatial-temporal cilia motion patterns in two-dimensional (2D) space. To improve the imaging speed, we recently introduced a new cilia imaging technique called spectral-encoded interferometric microscopy (SEIM). The SEIM system combines a wavelength sweeping laser source and a transmission diffraction grating to scan the sample and detect reflected light from multiple positions along the line-field simultaneously (29,30,33), which allows for 2D PRD measurement at speed comparable with OCT cross-sectional scans. Although SEIM does not have depth-resolved imaging capability, our previous studies indicate that SEIM imaging can successfully map out spatial-temporal ciliary activity over a 2D space on *ex vivo* ovary duct and tracheal tissue samples at high temporal and spatial resolution (29,30). SEIM is a promising technique for cilia imaging as it combines the advantage of high phase sensitivity in phase-resolve Doppler OCT, and high speed 2D imaging capability of traditional microscopy techniques. However, the main drawback of using Doppler measurement is that it is easily influenced by the artifacts generated by the sample bulk motion and the inherent phase noise of the laser. To overcome this challenge, we proposed an analysis method to

process PRD images acquired from the SEIM system that can filter out the phase noise and provide more distinctive visualization of the cilia motion.

In this study, we report the development of phase resolved dynamic wavefront imaging (PRDWI) technology based on the phase-resolved enhanced dynamic (PHRED) analysis of PRD images that enables 2D visualization and quantitative analysis of ciliary metachronal waves, in addition to extracting CBF and morphological information. To demonstrate the feasibility of this technique to visualize cilia movement clearly, PRD images were acquired from a freshly excised rabbit trachea using a previously configured SEIM system, PHRED analysis was then applied to several spatial locations on the PRD images. Finally, to validate the accuracy of the physiological parameters obtained from PHRED analysis, additional PRD images of *ex vivo* rabbit tracheal sample were acquired at 3 temperatures in increasing order from 25 to 37 ℃.

Methods

Theory of enhanced dynamic cilia imaging

The SEIM system combines a wavelength sweeping laser source and a transmission diffraction grating (WP-HD1145/1310, Wasatch Photonics, UT, USA) to detect reflected light from multiple positions along the line-field simultaneously (29,30,33). To acquire two-dimensional *en face* scanning, a single-axis galvanometer mirror was added to sweep the line-field illumination across the sample. Furthermore, by employing a reference optical path that interferes with the backscattered light, PRD measurement of cilia beating is possible (23,29,30), where instantaneous height changes Δz (t,x,y) during a ciliary beating cycle can be calculated from the relative phase shift $\Delta\phi(t,x,y)$ in the spectral interferences at one specific spatial location x,y and time t. Here, x represents location in the galvanometer scan direction and y in the wavelength scan direction. The relation between Δz and $\Delta\phi$ can be expressed as

$$\frac{\Delta\phi(t,x,y)}{2\pi}=\frac{2n\cdot\Delta z(t,x,y)}{\lambda_0} \quad [1]$$

where n is the refractive index of the mucosa layer, λ_0 is the center wavelength of the light source. The relative phase shift $\Delta\phi(t,x,y)$ can be estimated from subtracting the instantaneous phase of time-series 2D spectral interferograms $S_{t,x,y}$ acquired from SEIM imaging and can be expressed as

$$\Delta\phi(t,x,y)=\phi(t+\Delta t,x,y)-\phi(t,x,y) \quad [2]$$

where Δt is the time-interval between the successive *en face* scans. The instantons phase $\phi(t,x,y)$ of the spectral interferogram was obtained by deriving the analytical form $(C_{t,x,y})$ of the interferogram using Hilbert transform along the wavelength direction (y):

$$C_{t,x,y}=S_{t,x,y}+j\cdot Hilbert\left[S_{t,x,y}\right] \quad [3]$$

This was necessary as the recorded spectral interferograms from SEIM contains only the real values. Then, the instantaneous phase was estimated from the analytical form using the cross-correlation method. To further improve the signal contrast of the phase-resolved image, we expanded the Eq. [2] by adding a 3D averaging kernel in x,y, and t direction. The full expression of the modified PRD calculation is shown as

$$\Phi_{t,x,y}=\tan^{-1}\left[\sum_{t=0}^{T-1}\left\{\sum_{j=0}^{J-1}\sum_{n=0}^{N-1}\frac{\mathrm{Im}\left(C_{t+1,j,n}\right)\mathrm{Re}\left(C_{t,j,n}\right)-\mathrm{Im}\left(C_{t,j,n}\right)\mathrm{Re}\left(C_{t+1,j,n}\right)}{\mathrm{Re}\left(C_{t,j,n}\right)\mathrm{Re}\left(C_{t+1,j,n}\right)+\mathrm{Im}\left(C_{t+1,j,n}\right)\mathrm{Im}\left(C_{t,j,n}\right)}\right\}\right] \quad [4]$$

where J and N denote the number of spatial points, T denotes the number of temporal points in the averaging kernel, and $\Phi_{t,x,y}$ indicates the resulting time-series 2D PRD images consists of $\Delta\phi(t,x,y)$. The large window size in the x,y direction effectively reduce the phase noises and enhance the PRD contrast without sacrificing the lateral resolution due to the high sampling density of the SEIM imaging system. We acquired 2,000×2,000 spatial points from a single *en face* scan of 550 μm × 550 μm, where the pixel resolution (0.27 μm) is much smaller than the lateral resolution (1.5 μm) of the imaging system.

Additionally, we developed a PHRED analysis method to obtain a phase-field representation of ciliary metachronal waves from the PRD images as shown in *Figure 1*. PHRED analysis performs spatial-temporal frequency analysis of the time-series PRD images over a short temporal window and extracts the phase value of a single dominant frequency at each spatial location, refer to as dynamic wavefront (DW) images.

The DW images correspond to the time-varying phase field of ciliary metachronal waves, where the direction and the coordination of metachronal motions can be clearly visualized. Mathematically, the Doppler power spectrum density function $P(t,x,y,\omega)$ within the sliding window can be described as

$$P(t,x,y,\omega)=\left|\int_t^{t+\sigma_{win}}\Phi_{t,x,y}\exp(-i\omega\tau)\,d\tau\right|^2 \quad [5]$$

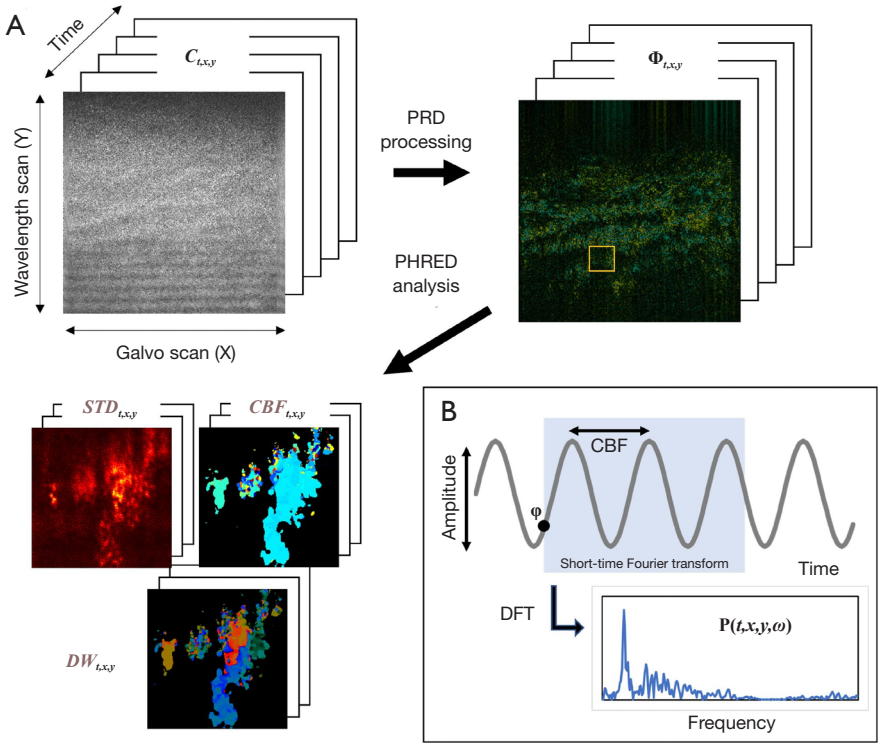

Figure 1 Data processing workflow. (A) Time-series 2D spectral interferograms are first converted to PRD images. Then, PHRED analysis is performed to extract dynamic wavefront, ciliary beating frequency, and beating amplitude maps. (B) The process of generating Doppler power spectrum density function from time-series PRD images in PHRED analysis. The time-varying PRD signal in each spatial location is converted to Doppler power spectrum density within a sliding window to estimate dominant frequency. The yellow box indicates the location of PHRED analysis. PRD, phase-resolved Doppler; PHRED, phase-resolved enhanced dynamic; STD, standard deviation; CBF, cilia beating frequency; DW, dynamic wavefront; DFT, discrete Fourier transform; 2D, two-dimensional.

where σ_{win} is the duration of short-time window from the N number of consecutive PRD images and N is empirically fixed to 100 frames in this study. In addition, an arbitrary thresholding value was applied to the Doppler power spectrum density to filter out the background. Then, the CBF and DW images were constructed from the dominant frequency of Doppler power spectrum density (ω_D) at each spatial location, where the resulting spatial-temporal maps can be expressed as

$$CBF_{t,x,y} = \omega_D \text{ where } P = \max\left[P(t,x,y,\omega)\right] \quad [6]$$

$$DW_{t,x,y} = angle\left[P(t,x,y,\omega)\right] \text{ where } \omega = \omega_D \quad [7]$$

Aside from the CBF and DW images, we obtained a 2D ciliary beating amplitude map by taking the standard deviation (STD) of the PRD images along the temporal axis at each spatial location shown as

$$STD_{t,x,y} = \sqrt{\frac{1}{N-1}\sum_{t=0}^{\sigma_{win}}\left(\Phi_{t,x,y} - \bar{\Phi}_{t,x,y}\right)} \quad [8]$$

Preparation of trachea explant culture

A tracheal sample from a healthy male New Zealand white rabbit weighing 4 kg was obtained by excising it immediately after the animal was euthanized with Euthasol injection. The use of animal in this experiment was reviewed and approved by the Institutional Animal Care and Use Committee at the University of California, Irvine, before the procedure. The tracheal sample was then dissected into a segment measuring 5 mm × 5 mm. To image the cilia, the sectioned tissue was placed in a petri dish that had a depression in the center and was filled with saline solution (*Figure 2*). The depressed region provided the chamber for housing the tissue and allowed for submersion of CO_2

Independent Medium (Thermo Fisher Scientific, Les Ulis, France). A microscope cover glass was placed on top of the silicone to provide a flat surface for SEIM imaging and to reduce movement caused by the water surface. The tissue is kept in the room temperature during the preparation.

System setup and implementation

Our phase-resolved cilia imaging system is based on the fiber-based swept-source SEIM setup presented previously (29,30) (*Figure 3*). The imaging system was built with a vertical-cavity surface-emitting laser (MEMS-VCSEL, Thorlabs, NJ, USA) that operates at a center wavelength of 1,310 nm, has a bandwidth of 100 nm, and a repetition rate of 100 kHz. A 90:10 fiber coupler is used to divide the laser output into the sample and reference arm in the Mach-Zehnder interferometer. Each arm has a circulator that directs the illumination light to the sample or reference mirror and the returning light to a 50:50 coupler and a balanced photodetector, which produces the interferograms. In the sample arm, once the light from the optical fiber is collimated, a transmission diffraction grating spatially disperses the illumination light into different wavelengths where each wavelength encodes a successive location on a transverse line (x-scan). *En face* scanning is achieved by using a galvanometer mirror interposed between the two 4F relay lens pairs (L1 pair and L2 pair) to move the spectrally dispersed line illumination across the imaging field in the slow axis. The sample illumination power was 3 mW. The first pair of lenses, designated L1, is made up of achromatic doublets with a focal length of 35mm. The second pair of lenses, designated L2, serves as a beam expander by having a focal length of 35 mm and L2' having a focal length of 50 mm. This allows the laser beam to fill the entrance pupil of the objective lens, thus maximizing the lateral resolution. The galvanometer mirror, which is driven by a sawtooth waveform, can operate at a frequency of up to 200 Hz.

A 20× apochromat objective lens with a 0.40 numerical aperture (MY20X-824, Mitutoyo Corporation, Japan) was used to capture the micromotion of cilia and provide high lateral resolution. The reference arm consists of compensating windows for offsetting dispersion and a gold mirror. The interferograms generated by the returning reference and sample signals were converted into electrical signals via a balanced photodetector and then acquired using a waveform digitizer. The digitized signals were then processed using a GPU. The system has

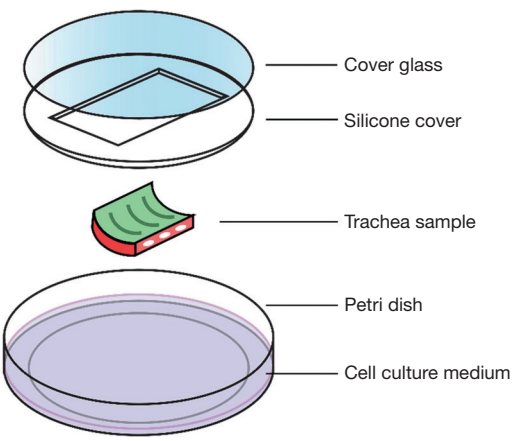

Figure 2 Custom imaging chamber for a cilia explant.

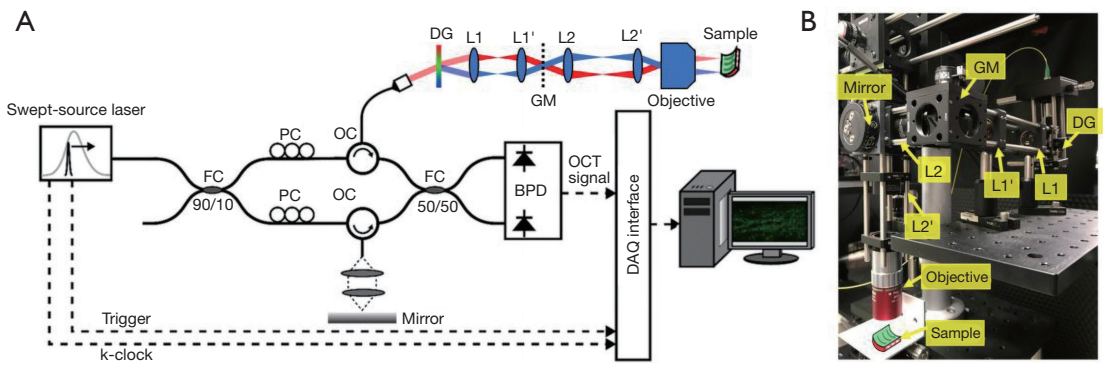

Figure 3 SEIM system setup. (A) Schematic diagram of SEIM imaging system. (B) Optomechanical arrangement of the sample arm. SEIM, spectral-encoded interferometric microscopy; L, lens; PC, polarization controller; FC, fiber coupler; DG, diffractive grating; BPD, balanced photodetector; OC, optical circulator; GM, galvanometer mirror; OCT, optical coherence tomography; DAQ, data acquisition.

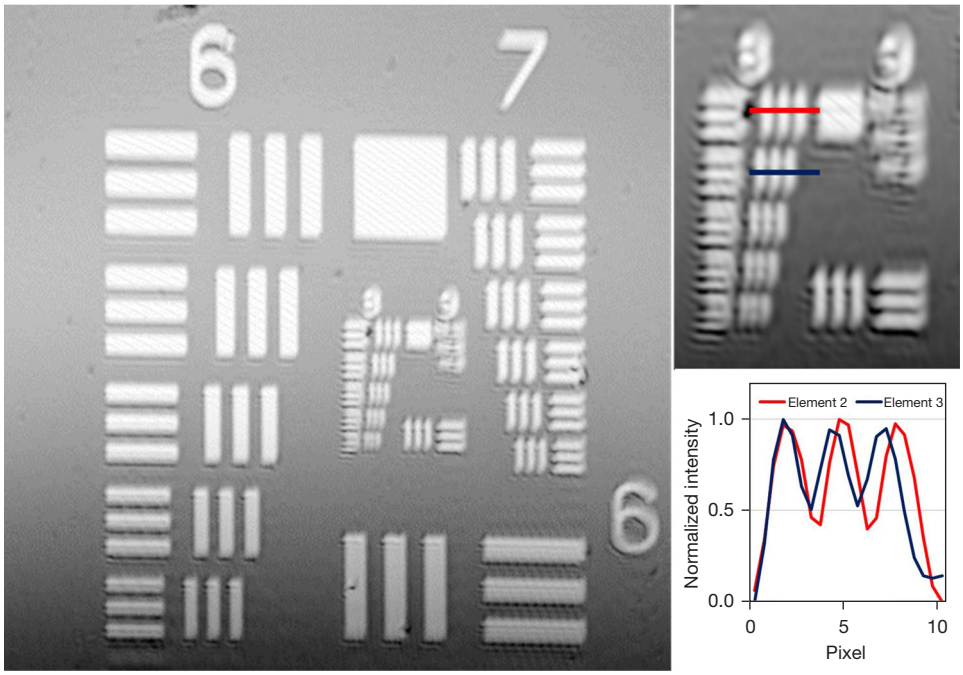

Figure 4 A resolution test target imaged with the SEIM system, showing Element 2 of Group 8 can be resolved. SEIM, spectral-encoded interferometric microscopy.

a field of view of 550×550 μm^2 and a lateral resolution of approximately 1.5 μm, determined using a 1951 U.S. Air Force (USAF) resolution target. A 1951 USAF resolution target, commonly used to determine the optical resolution of a microscope, contains groups of small target features, each with a specific spatial frequency. The target contains 9 groups, each comprising of 6 elements, with varying feature dimensions. The largest element with non-distinguishable lines determines the spatial resolution limit of the optical system. *Figure 4* shows an image of a 1951 USAF resolution target showing Element 2 of Group 8 can be distinguished but not the Element 3.

Results

To demonstrate that PHRED technique can resolve metachronal waves, time-series spectral interferograms were acquired from an *ex vivo* tracheal explant culture harvested from a healthy rabbit airway. Before the image acquisition, the *ex vivo* trachea explant was carefully placed in a custom-designed imaging dish with the lumen side facing the objective lens. We obtained total of 500 images at 50 frame-per-second, with each *en face* image consists of 2,000×2,000 number of pixels. As the PRD signal is sensitive to the motion and phase noises, we apply trigger jittering correction and bulk motion correction before the PRD estimation (34). Time-series PRD images of rabbit trachea are shown in *Figure 5*, where the area of active ciliary motion can be visualized and color-coded based on the PRD values (ϕ). Presence of active cilia movement can be observed along the direction of tracheal cartilage as the location of strong PRD signal. However, it is difficult to discern the coordination and the presence of the metachronal waves from the PRD images. Next, three representative locations (shown as yellow, blue, orange boxes in *Figure 5A* are selected for PHRED analysis. In *Figure 5B*, the PHRED analysis revealed different dynamics of ciliary motion at each region-of-interest (ROI), where three distinct ciliary patches can be identified. In ROI 1, the largest cilia patch on the right exhibit mostly uniform CBF around 3.4 Hz. Contrary to the CBF map, the largest cilia path in ROI 1 exhibit different color in the DW images. While the top part of the patch shows a red color, the bottom part of the same patch shows a blue color. This agrees well with the characteristics of coordinated cilia beating pattern, where the cilia will have the same characteristic beating frequency but in a phase-shifted manner compared to their neighbors (6). The STD of the Doppler amplitude shows

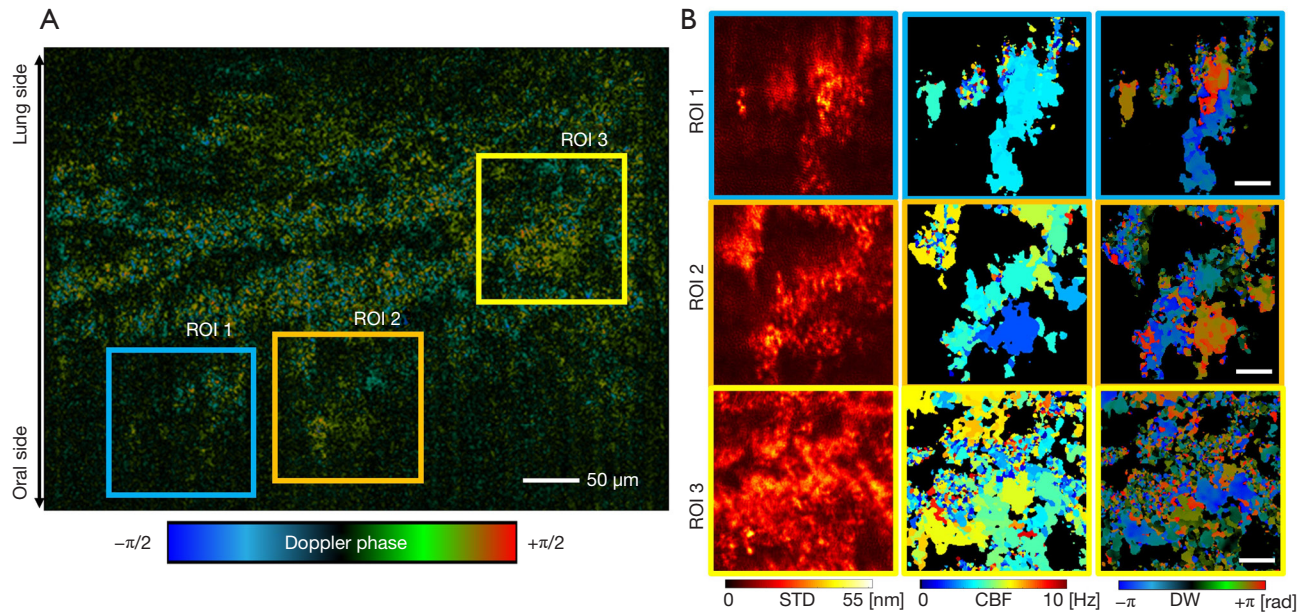

Figure 5 Analysis results of a rabbit tracheal tissue explant. (A) Phase-resolved Doppler image of the tracheal tissue. (B) Phase-resolved enhanced dynamic analysis of selected ROIs. Scale bars indicate 20 μm. ROI, region-of-interest; STD, standard deviation; CBF, cilia beating frequency; DW, dynamic wavefront.

well-defined shape of cilia patches, confirming the well-coordinated cilia beating motion. On the other hand, the middle ciliary patch exhibits random CBF and phase, indicating uncoordinated ciliary beating. In addition, the beating amplitude is blurred out in the STD plot, indicating the randomized and overlapping beating motion. Finally, the ciliary patch on the left shows similar behavior as the largest patch, beating at 4.1 Hz. However, the DW image does not show a specific directionality due to the small size of the patch.

In ROI 2, the adjacent patches on the lower side of the images have two distinct CBF, one beating at 4.1 Hz and the other beating at 2.0 Hz. Although the two patches have distinct CBF, the ciliary motion in one side can affect the other side, including changing the CBF distribution, as shown in *Figure 6*. Finally, ROI 3 shows the portion of cilia patch with less coordination compared to the previous two locations. The STD image indicates overall larger amplitude compared to the other two areas close to the center, however, the CBF and DW images suggests the movement is largely random and not well coordinated. The relatively slow CBF observed in our study can be explained by the low temperature of buffer solution as CBF is known to have temperature dependency (23). During the preparation and the imaging, the tissue sample was kept in a buffer solution at room temperature rather than the physiological temperature.

Discussion

Qualitative comparison of PRD and DW images

The DW images revealed spatial variance of the beating cycle at high fidelity compared to the PRD images. In PRD images, the wave propagation was difficult to identify due to the low signal-to-noise ratio and various phase noises (see Video S1). On the other hand, the orientation and the speed of the metachronal wave can be clearly identified in DW images (see Video S1). We found that one merit of using the PHRED analysis is that it effectively eliminates the phase noise present in the PRD images by focusing on only the primary frequency component of the signal. It is well known that Doppler phase detection is inherently sensitive to the phase stability and noise of the light source, internal and external motion artifacts, stability of detection system, and variation in the optical aberrations (34). Finally, we demonstrated the temporal variation in the metachronal wave propagation direction within the same cilia patch (*Figure 7*). In one time point, the wave propagation is along the vertical direction (yellow

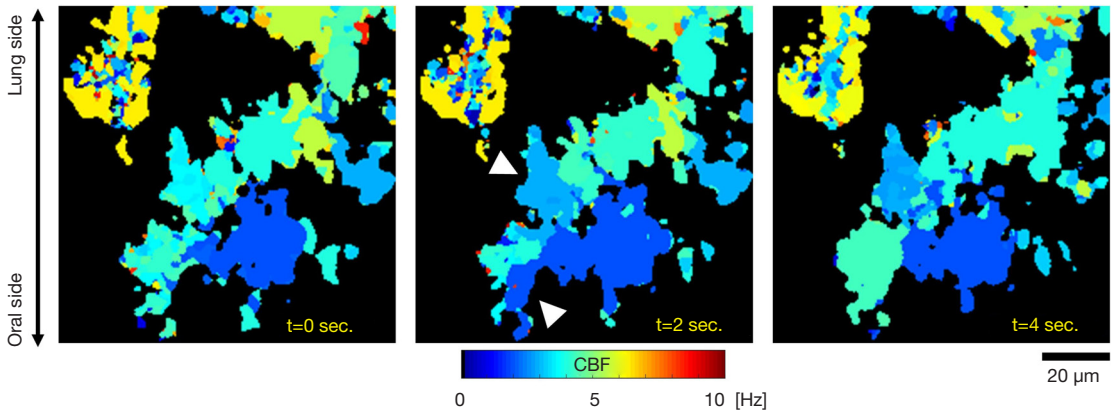

Figure 6 Changes in the CBF map over time at ROI 2. The white arrowheads indicate the areas that have most noticeable changes in the CBF distribution. Black areas correspond to the parts with weak cilia beating amplitude. CBF, cilia beating frequency; ROI, region-of-interest.

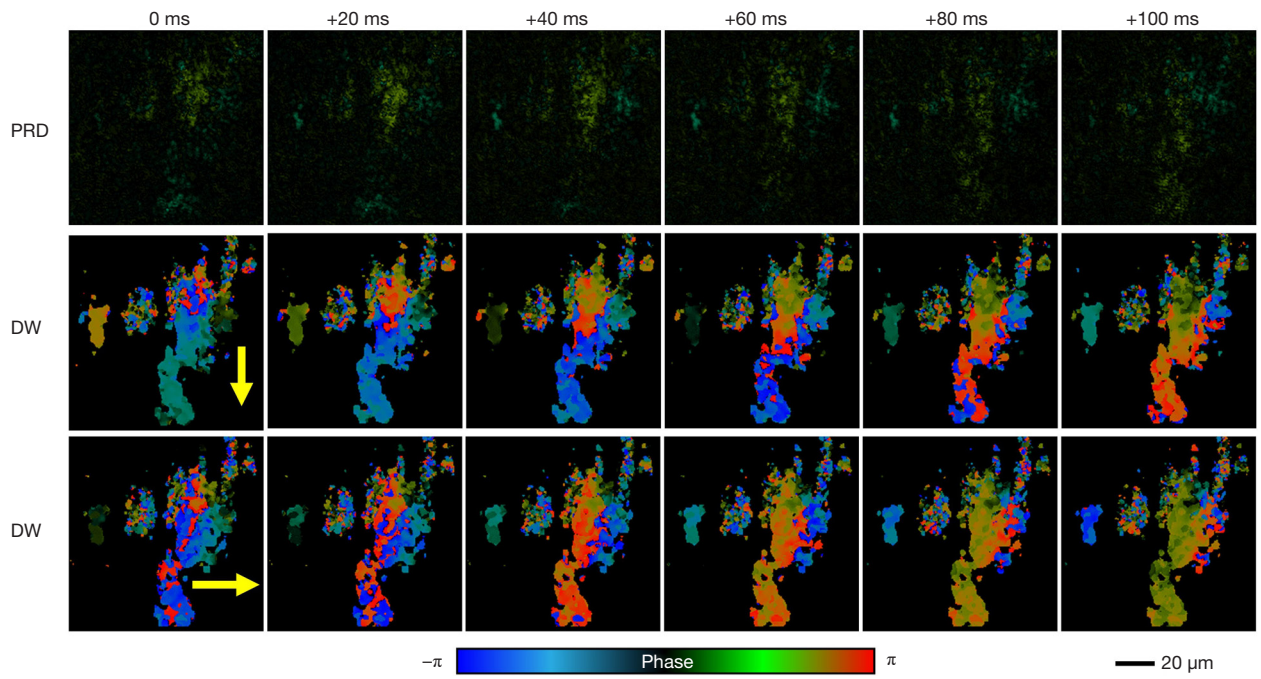

Figure 7 Visualization of dynamic wavefront and metachronal wave propagation at ROI 1. Yellow arrows in the dynamic wavefront images indicate the direction of metachronal wave propagation. Metachronal waves can hardly be resolved in the time-series phase-resolved Doppler images. See Video S1. PRD, phase-resolved Doppler; DW, dynamic wavefront; ROI, region-of-interest.

arrow in the middle row). In another time point, the wave propagation changes to the horizonal direction (yellow arrow in the bottom row). This indicates the direction of metachronal wave propagation may be constantly changing during the mucus transport rather than having a certain transportation path.

Characterization of temperature dependency on CBF

To evaluate the effects of different temperatures on CBF in a rabbit trachea, we acquired PRD images and analyzed CBF through PHRED analysis while setting the temperature of the base plate to 25, 32, and 37 ℃. The sample preparation

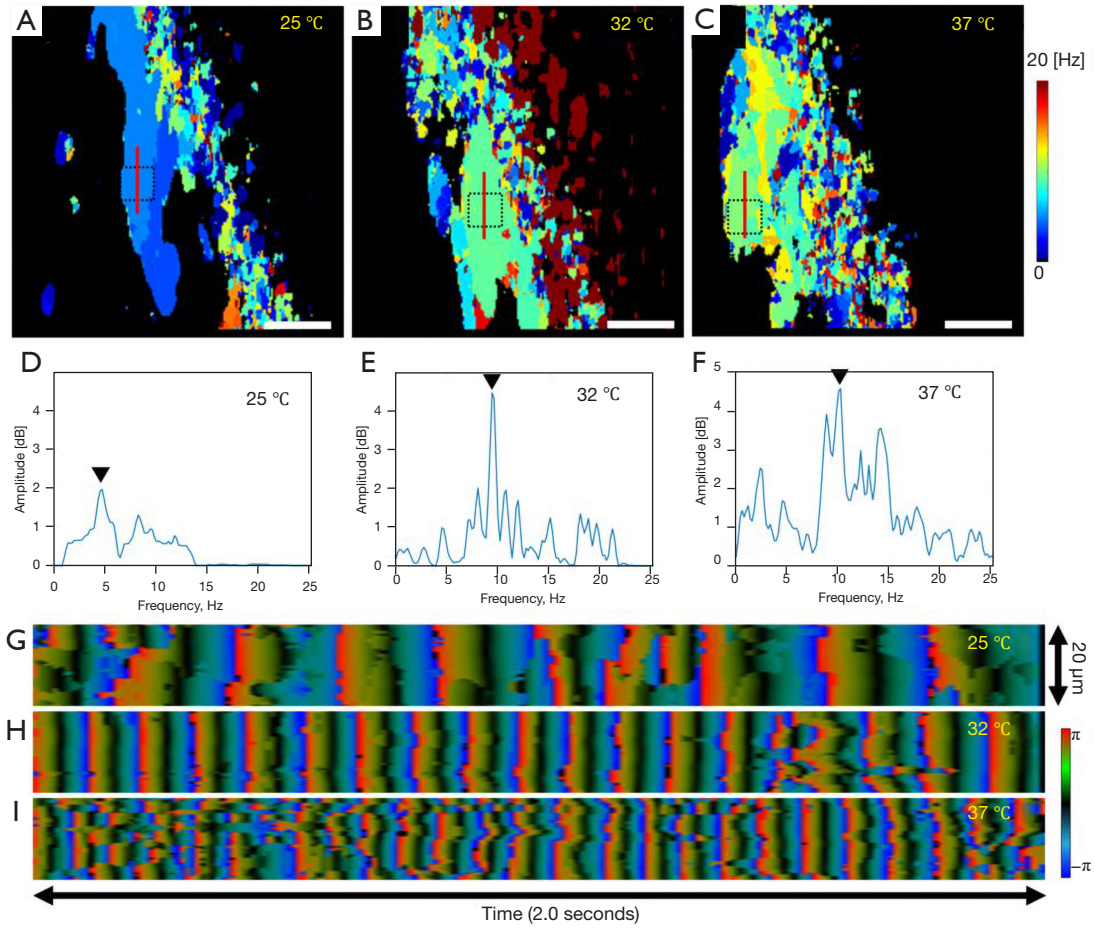

Figure 8 Analysis of the cilia beating characteristics at different temperatures. (A-C) Spatial distribution of cilia beating frequency map at 25, 32, and 37 ℃. (D-F) Doppler power spectrum density function profiles at the location indicated by the dotted boxes, where the peak (black triangles) corresponds to the dominant CBF. (G-I) Temporal changes of phase in dynamic wavefront images at the location indicated by the red lines in (A-C). Scale bars indicate 20 μm. CBF, cilia beating frequency.

follows the same procedure described in the method section, except that the tissue sample is placed on a temperature-programmable heating plate in this measurement. *Figure 8A-8C* displays a CBF map of the rabbit tracheal sample taken at the fixed location at various temperatures. The colors represent the CBF value, with black denoting the locations with minimum cilia movement. At each temperature, we can observe a connected area containing a single CBF frequency near the area marked by black dotted lines. Based on our result, a coordinated cilia movement (e.g., metachronal wave) can be easily observed from these areas. *Figure 8D-8F* shows the Doppler power spectrum density of the area indicated by dotted lines in *Figure 8A-8C*. We found the dominant frequencies of each temperature are 4.8±1.6, 9.7±1.6, 10.2±0.8 Hz at 25, 32, and 37 ℃, respectively. It is worth noting that these CBF values in rabbit trachea closely match our previous study (23). Finally, we generated DW images for each temperature condition and visualized the phase changes in the DW images at a fixed spatial location over time. *Figure 8G-8I* shows the phase changes in DW images at the locations indicated by the solid red lines in *Figure 8A-8C* over the time duration of 2 seconds. The temporal changes of the phase in DW images clearly show a higher modulation frequency of cilia beating as the temperature increases.

Future directions

Although the frame acquisition rate of SEIM imaging system can reach more than 200 Hz, the frame rate in

this study was set to 50 Hz based on the ciliary beating frequency range of rabbit trachea, which provided a good trade-off between acquisition speed (20 ms/frame) and signal-to-noise ratio in the PRD images. Combined with faster imaging speed of SEIM system compared to the point-by-point laser scanning-type microscopes, PHRED analysis is able to visualize cilia movement over a relatively wide field-of-view while maintaining high imaging frame rate, which is important to capture the full dynamics of metachronal wave propagation. Future studies will involve investigating the critical questions regarding the formation and the stability of metachronal waves; such as, what is the stability of metachronal wave coordination and directional orders over time? How does the formation of metachronal wave affected by the spatial and geometrical arrangement of the cilia? In addition, the sample arm of the SEIM system can potentially be configured to a handheld endoscope by replacing the objective lens rod with a gradient index lens, similar to the design demonstrated in one of our previous studies (35).

Conclusions

In conclusion, we have demonstrated that SEIM system combined with PHRED analysis provides a new tool to study collective ciliary interaction and characterize organized cilia motion. The feasibility of the PRDWI technique has been verified through acquiring data from freshly excised rabbit trachea tissue with varying temperatures. Continued development of this technique, including configuring the sample arm into a handheld endoscope, can expand the clinical and utility of this technique and provide insight into the biological mechanism of the coordinated ciliary beating.

Acknowledgments

The authors would like to thank David Mukai and George Philipopoulos for their contributions to the preparation of the sample.
Funding: This study was supported by the National Institutes of Health (Nos. R01EB-030024, R01HL-125084, R01EB-030558, R01EY-026091); Air Force Office of Scientific Research (No. FA9550-20-1-0053); CounterACT Program, National Institutes of Health, Office of the Director, and the National Institute of Environmental Health Sciences (No. U54 ES027698).

Footnote

Conflicts of Interest: All authors have completed the ICMJE uniform disclosure form (available at https://qims.amegroups.com/article/view/10.21037/qims-22-439/coif). The authors have no conflicts of interest to declare.

Ethical Statement: The authors are accountable for all aspects of the work in ensuring that questions related to the accuracy or integrity of any part of the work are appropriately investigated and resolved. Ethical approval and written informed consent are not applicable to this study as it does not involve human subjects and/or tissues derived from human.

References

1. Wanner A, Salathé M, O'Riordan TG. Mucociliary clearance in the airways. Am J Respir Crit Care Med 1996;154:1868-902.
2. Tilley AE, Walters MS, Shaykhiev R, Crystal RG. Cilia dysfunction in lung disease. Annu Rev Physiol 2015;77:379-406.
3. Salathe M. Regulation of mammalian ciliary beating. Annu Rev Physiol 2007;69:401-22.
4. Sanderson MJ, Sleigh MA. Ciliary activity of cultured rabbit tracheal epithelium: beat pattern and metachrony. J Cell Sci 1981;47:331-47.
5. Teff Z, Priel Z, Gheber LA. Forces applied by cilia measured on explants from mucociliary tissue. Biophys J 2007;92:1813-23.
6. Elgeti J, Gompper G. Emergence of metachronal waves in cilia arrays. Proc Natl Acad Sci U S A 2013;110:4470-5.
7. Yaghi A, Dolovich MB. Airway Epithelial Cell Cilia and Obstructive Lung Disease. Cells 2016;5:40.
8. Winters SL, Yeates DB. Interaction between ion transporters and the mucociliary transport system in dog

and baboon. J Appl Physiol (1985) 1997;83:1348-59.
9. Chilvers MA, Rutman A, O'Callaghan C. Functional analysis of cilia and ciliated epithelial ultrastructure in healthy children and young adults. Thorax 2003;58:333-8.
10. Kempeneers C, Seaton C, Garcia Espinosa B, Chilvers MA. Ciliary functional analysis: Beating a path towards standardization. Pediatr Pulmonol 2019;54:1627-38.
11. Hirst RA, Rutman A, Williams G, O'Callaghan C. Ciliated air-liquid cultures as an aid to diagnostic testing of primary ciliary dyskinesia. Chest 2010;138:1441-7.
12. Lodes N, Seidensticker K, Perniss A, Nietzer S, Oberwinkler H, May T, Walles T, Hebestreit H, Hackenberg S, Steinke M. Investigation on Ciliary Functionality of Different Airway Epithelial Cell Lines in Three-Dimensional Cell Culture. Tissue Eng Part A 2020;26:432-40.
13. Feriani L, Juenet M, Fowler CJ, Bruot N, Chioccioli M, Holland SM, Bryant CE, Cicuta P. Assessing the Collective Dynamics of Motile Cilia in Cultures of Human Airway Cells by Multiscale DDM. Biophys J 2017;113:109-19.
14. Bustamante-Marin XM, Ostrowski LE. Cilia and Mucociliary Clearance. Cold Spring Harb Perspect Biol 2017.
15. Burn A, Schneiter M, Ryser M, Gehr P, Rička J, Frenz M. A quantitative interspecies comparison of the respiratory mucociliary clearance mechanism. Eur Biophys J 2022;51:51-65.
16. Gardner M, Parsons D, Morgan K, McCarron A, Cmielewski P, Gradl R, Donnelley M. Towards automated in vivo tracheal mucociliary transport measurement: Detecting and tracking particle movement in synchrotron phase-contrast x-ray images. Phys Med Biol 2020;65:145012.
17. Donnelley M, Morgan KS, Gradl R, Klein M, Hausermann D, Hall C, Maksimenko A, Parsons DW. Live-pig-airway surface imaging and whole-pig CT at the Australian Synchrotron Imaging and Medical Beamline. J Synchrotron Radiat 2019;26:175-83.
18. Morgan KS, Donnelley M, Farrow N, Fouras A, Yagi N, Suzuki Y, Takeuchi A, Uesugi K, Boucher RC, Siu KK, Parsons DW. In vivo X-ray imaging reveals improved airway surface hydration after a therapy designed for cystic fibrosis. Am J Respir Crit Care Med 2014;190:469-71.
19. Jonas S, Bhattacharya D, Khokha MK, Choma MA. Microfluidic characterization of cilia-driven fluid flow using optical coherence tomography-based particle tracking velocimetry. Biomed Opt Express 2011;2:2022-34.
20. Lemieux BT, Chen JJ, Jing J, Chen Z, Wong BJ. Measurement of ciliary beat frequency using Doppler optical coherence tomography. Int Forum Allergy Rhinol 2015;5:1048-54.
21. Leung HM, Birket SE, Hyun C, Ford TN, Cui D, Solomon GM, Shei RJ, Adewale AT, Lenzie AR, Fernandez-Petty CM, Zheng H, Palermo JH, Cho DY, Woodworth BA, Yonker LM, Hurley BP, Rowe SM, Tearney GJ. Intranasal micro-optical coherence tomography imaging for cystic fibrosis studies. Sci Transl Med 2019.
22. Shei RJ, Peabody JE, Rowe SM. Functional Anatomic Imaging of the Airway Surface. Ann Am Thorac Soc 2018;15:S177-83.
23. Jing JC, Chen JJ, Chou L, Wong BJF, Chen Z. Visualization and Detection of Ciliary Beating Pattern and Frequency in the Upper Airway using Phase Resolved Doppler Optical Coherence Tomography. Sci Rep 2017;7:8522.
24. Chen JJ, Jing JC, Su E, Badger C, Coughlan CA, Chen Z, Wong BJF. Measurement of ciliary beat frequency using ultra-high resolution optical coherence tomography. Proc SPIE 9689 Ther Diagnostics XII 2016;9689:968926.
25. Cui D, Chu KK, Yin B, Ford TN, Hyun C, Leung HM, Gardecki JA, Solomon GM, Birket SE, Liu L, Rowe SM, Tearney GJ. Flexible, high-resolution micro-optical coherence tomography endobronchial probe toward in vivo imaging of cilia. Opt Lett 2017;42:867-70.
26. Pieper M, Schulz-Hildebrandt H, Mall MA, Hüttmann G, König P. Intravital microscopic optical coherence tomography imaging to assess mucus-mobilizing interventions for muco-obstructive lung disease in mice. Am J Physiol Lung Cell Mol Physiol 2020;318:L518-24.
27. Liu L, Chu KK, Houser GH, Diephuis BJ, Li Y, Wilsterman EJ, Shastry S, Dierksen G, Birket SE, Mazur M, Byan-Parker S, Grizzle WE, Sorscher EJ, Rowe SM, Tearney GJ. Method for quantitative study of airway functional microanatomy using micro-optical coherence tomography. PLoS One 2013;8:e54473.
28. Ansari R, Buj C, Pieper M, König P, Schweikard A, Hüttmann G. Micro-anatomical and functional assessment of ciliated epithelium in mouse trachea using optical coherence phase microscopy. Opt Express 2015;23:23217-24.
29. He Y, Qu Y, Jing JC, Chen Z. Characterization of oviduct ciliary beat frequency using real time phase resolved Doppler spectrally encoded interferometric microscopy. Biomed Opt Express 2019;10:5650-9.
30. He Y, Jing JC, Qu Y, Wong BJ, Chen Z. Spatial mapping of tracheal ciliary beat frequency using real time phase-

resolved Doppler spectrally encoded interferometric microscopy. ACS Photonics 2020;7:128-34.
31. de Boer JF, Srinivas SM, Park BH, Pham TH, Chen Z, Milner TE, Nelson JS. Polarization Effects in Optical Coherence Tomography of Various Biological Tissues. IEEE J Sel Top Quantum Electron 1999;5:1200-4.
32. Yelin D, Bouma BE, Rosowsky JJ, Tearney GJ. Doppler imaging using spectrally-encoded endoscopy. Opt Express 2008;16:14836-44.
33. Tearney GJ, Webb RH, Bouma BE. Spectrally encoded confocal microscopy. Opt Lett 1998;23:1152-4.
34. Moon S, Chen Z. Phase-stability optimization of swept-source optical coherence tomography. Biomed Opt Express 2018;9:5280-95.
35. Coughlan CA, Chou LD, Jing JC, Chen JJ, Rangarajan S, Chang TH, Sharma GK, Cho K, Lee D, Goddard JA, Chen Z, Wong BJ. In vivo cross-sectional imaging of the phonating larynx using long-range Doppler optical coherence tomography. Sci Rep 2016;6:22792.

Cite this article as: Miao Y, Jing JC, Chou L, Zhu Z, Wong BJF, Chen Z. Phase-resolved dynamic wavefront imaging of cilia metachronal waves. Quant Imaging Med Surg 2023;13(4):2364-2375. doi: 10.21037/qims-22-439

